Silicon
https://doi.org/10.1007/s12633-024-03076-8

RESEARCH

Efficiency Boosting of 4-T Bifacial Dual-Textured Perovskite/Perl Silicon Tandem Solar Cells: Process and Device TCAD Simulation Study

H. A. El-Demsisy[1] · Ahmed Shaker[2] · M. D. Asham[1] · Ibrahim S. Ahmed[1] · Tarek M. Abdolkader[1]

Received: 18 April 2024 / Accepted: 22 June 2024

Abstract
Perovskite/Silicon tandem solar cells have earned substantial attention in the field of photovoltaics (PVs) due to their potential high-efficiency energy conversion. The provided TCAD simulation in the current work aims at delivering a novel design for a 4-T Perovskite/PERL p-type Si tandem solar cell. The main structure consists of ITO/CuSCN/Perovskite/PC60PM/AZO/AgNW as the top cell and a conventional PERL p-Si as the bottom cell. Simulation results showed that the proposed top cell structure achieves a significant performance after substituting $Zn(O_{0.3},S_{0.7})$ for AZO and PC60PM electron transport layers (ETLs), while replacing CuSCN with CuI as a suitable alternative for the hole transport layer (HTL). These modifications achieved an efficiency of 19.81% for the top cell. The bottom cell also attained a noteworthy level of performance by using bifacial dual-side-textured construction with efficiencies reaching 29.11% and 14.08% for bare and filtered cells, respectively. With these combined modifications, the PCE (power conversion efficiency) reached 33.89%, showing significant improvement compared to the base structure.

Keywords 4-T Bifacial tandem solar cell · CBO · VBO · Perovskite · Perl Si · TCAD simulation

1 Introduction

Environmental pollution resulting from fossil and nuclear fuels results in catastrophic impacts on earth's eco-system. These effects may outstretch human psychological traumas to endangering life on the planet as a whole [1–4]. To tackle this crisis, humanity needed to embrace renewable, clean energy sources to restore the environment. Wind power, biomass and solar energy have been the most notable candidates for this purpose over the last few decades [5–7]. Solar energy is the foremost among these available renewable resources. In this regard, single-junction PV cells have spread on a large scale as the dominant technology for harvesting solar energy and converting it into electricity. Nevertheless, these cells face some challenges in their limited power conversion efficiency (PCE) bounded by the Shockley-Quiesser limit (33%) [8]. This led solar-cell technology to shift towards multi-junction designs to be able to realize higher efficiencies.

The main basic factor known to limit the efficiency of single-junction cells is either the insufficiency or the excess of the photon energy compared to that of the bandgap of the absorption layer (or the active layer). The former results in a deficiency in photon absorption, while the latter leads to thermalization losses, where excess energy is lost as excited electrons relax from higher states of the conduction band to lower ones. Thus, to resolve the problem, it has been suggested to combine multiple absorbent materials with different bandgaps in multi-junction devices, thus evolving the "tandem solar-cell" structures [9, 10]. Tandems are the simplest way to garner much of the spectrum of the sun. In these cells, a front sub-cell with a high bandgap is used to absorb photons with high energy, followed by a rear sub-cell with a lower bandgap to absorb low energy photons.

Perovskite (PVK) materials are the best contenders for the top sub-cells for tandem structure for their distinguished optoelectronic properties. They have acquired the largest share of the optoelectronic energy arena due to their high efficiency alongside other multiple advantages such as high absorption coefficient, low Urbach energy [11], long carrier diffusion length [12], decent mobility [13] and most of

✉ H. A. El-Demsisy
hind.eldemssesy@bhit.bu.edu.eg

[1] Department of Basic Engineering Sciences, Benha Faculty of Engineering, Benha University, Benha, Egypt

[2] Department of Engineering Physics and Mathematics, Faculty of Engineering, Ain Shams University, Cairo, Egypt

Published online: 13 July 2024

all, tunable bandgap (1.18–2.3 eV) [14, 15]. For the bottom cell, the best material choice was found to be silicon due to its dominance in the market in terms of low cost, high efficiency [16, 17], appropriate low band gap (1.1 eV) [18] and high open-circuit voltage (V_{oc}) (up to 0.75 V) [19]. Notably, perovskite solar cells can be configured as (p-i-n) or (n-i-p) heterojunction structures or (p-n) homojunction structures [20, 21].

Numerous research investigations have been focused on improving both the design and performance of solar cells to reduce production costs and typical losses mechanisms with highest gainable efficiencies as the main scope to achieve. In this vein, innovative PV cell designs have been developed and studied. Three major groups of silicon-based cell structures are rated for the highest conversion efficiencies; a) Silicon Heterojunction (SHJ), b) Passivated Emitter, rear Locally diffused (PERL) and c) Interdigitated Back Contact (IBC) solar devices. In 1990, a PERL cell demonstrated a PCE of 23.1% [16, 22, 23]. The improved surface passivation is what distinguishes these cells from conventional ones as it reduces the emitter saturation current density and thus increases V_{oc}, which is shown by thermally grown oxide in the surrounding trichloroethane (TCA) [20]. In 1993, PERL cells were improved when the passivation of the front and rear contact areas was applied by the densely diffusion phosphorous and boron areas along with the passivation of TCA oxide for the front and back surfaces of the cell. Many other enhancements, including the reduction of contact areas, that led to a cutback in recombination rate at the contact contributing to the possibility of increasing V_{oc}. The textured upper surface with inverted-pyramid structures covering with a double anti-reflective coating (ARC) is the most important characteristic of these cells to reduce the upper surface cell reflection and recombination rate. Currently, PERL solar cells produce efficiencies approaching 25% using microtechniques under the standard AM1.5 spectrum [24–26]. Despite these high efficiencies, there are opportunities for further improvement by trapping light with double-sided pyramidal textures which are found to be more capable of trapping light than one-sided texture cells [27, 28]. Energy yield (EY) modeling is also particularly important, since the effect of albedo radiation harvested through bottom silicon cells greatly affects the performance of bifacial tandem cells.

Two out of the three main configurations of perovskite/c-silicon tandem solar-cells are of special interest: the two-terminal (2-T, or monolithic) cells and the four-terminal (4-T) cells. The two cell configurations differ in several aspects in terms of manufacturing, and handling of short circuit current (J_{sc}) and V_{oc}. In 4-T tandem cells, the top semi-transparent cell is mechanically assembled on top of the bottom cell, unlike 2-T tandems where all the layers of the two PV cells are successively deposited on each other. The two sub-cells in 4-T tandem architectures are also electrically isolated from one another, hence, no need for an optimal thickness to accomplish current matching. Alternatively, current matching must inevitably be applied for 2-T tandem cells. The latter should also be more transparent as it has a smaller number of transparent electrodes which helps in reducing losses caused by parasitic absorption and reflection [29, 30]. Furthermore, enhanced light management is more achievable with 4 T tandems than 2 T counterparts, thanks to advanced techniques such as dual-side texturing, which improve light absorption and efficiency. In addition, the electrical separation of the cells in a 4 T tandem means that degradation or failure of one cell does not necessarily impact the performance of the other, resulting in more reliable solar cells.

In 2014, the first 4-T tandem cell with perovskite was reported by Löper et al., with efficiency up to 13.4%, where it consisted of two sub-cells: perovskite and c-silicon heterojunction cells with MoOx/ITO as a transparent electrode [31]. Bailie et al. [32] have used a transparent electrode made of silver nanowire (NW) to build semitransparent perovskite solar cells (PSCS). Ramírez Quiroz followed Bailie's steps in using a semi-transparent silver nanowire (AgNW) rear-electrode on the top perovskite cell (PSCS) to make it semi-transparent. To evade the degradation of the device and prevent the diffusion of silver into the perovskite layer, Ramírez inserted AZO nanoparticles between the PC60BM and the silver nanowires. The CuSCN was also chosen by Ramírez to serve as an HTL and ARC as it has a refractive index that is close to that of perovskite materials in the NIR region and thus reduces parasitic absorption [33]. Device architecture for the top perovskite semi-transparent cell chosen by Ramírez was ITO/CuSCN/$CH_3NH_3PbI_3$/PC60BM/ZnO:Al nps/AgNW. On the other side, an inverted pyramidal texture is applied to a PERL p-type Si bottom cell to reduce light reflection. As a result, the total efficiency for the 4-T PSC/PERL p-type Si tandem cell is estimated at 26.7% when the semitransparent PSC (17.1%) is mechanically stacked to the PERL p-silicon solar cell (9.6%).

Our study addresses significant gaps in the literature on tandem solar cell configurations by integrating both process and device simulations, a comprehensive approach rarely explored in existing research. Most studies focus primarily on device simulations, neglecting the critical role of process simulations in accurately constructing and optimizing solar cell structures. Additionally, the impact of ARC and dual-textured surfaces on device performance has not been fully examined. In this simulation study, we present a novel 4 T Perovskite/Perl p-Si tandem PV cell featuring a bifacial double-sided pyramid texture model covered by a dual-layer ARC on both sides of the Perl p-Si bottom cell. Our study employs the Silvaco simulation package (Athena and Atlas) to conduct both process and device simulations, ensuring a detailed and accurate

modeling approach. The top and bottom cells were calibrated with experimental data from previous studies to validate the physical models and technological parameters used in the simulations. To improve tandem performance, a series of optimization steps have been performed. Firstly, we investigated the impact of various Conduction Band Offsets (CBOs) and Valence Band Offsets (VBOs) for different Electron Transport Layers (ETLs) and Hole Transport Layers (HTLs) in the top perovskite solar cell, leading to a significant improvement in efficiency from 17.4% to 19.81%. Next, for the bottom cell, we implemented some strategies to enhance light trapping and reduce reflection: anti-reflective coating and dual-side-textured surfaces. These techniques resulted in substantial efficiency gains, with the bottom cell's efficiency reaching 29.11% (bare cell) and 14.08% (filtered cell), compared to initial efficiencies of 23.5% and 10.08%, respectively. Modifications to the cells under study included creating an effective light trapping system, which further enhanced the overall performance of the tandem solar cell.

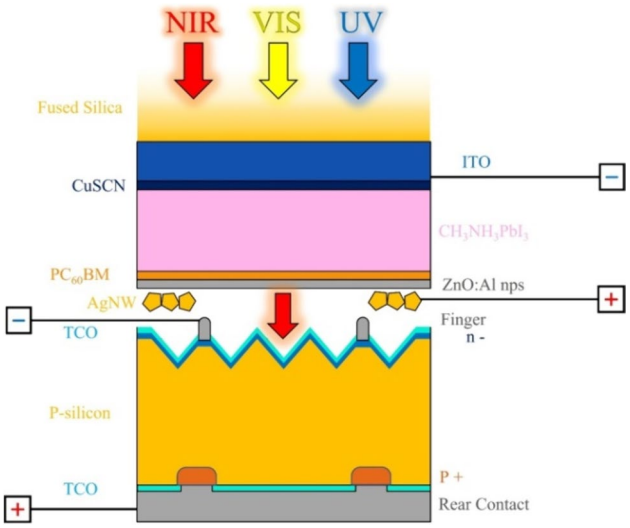

Fig. 1 Schematic representation of 4-terminal layout showing illumination direction with the silicon PERL cell as bottom cell [33]

2 Modeling, Simulation Methods and Cell Structures

SILVACO-TCAD modeling and simulation software packages play an important role in developing new solar structures under different operating conditions and predicting their performance with ease and expeditiousness. It is always preferable to design the device via a TCAD simulation tool prior to manufacturing to anticipate design issues or other avoidable problems that can help to maximize performance parameters [34]. Silvaco TCAD provides a comprehensive, flexible, and powerful simulation environment. Its superior process simulation capabilities, extensive material libraries, advanced physical models, 2D simulation capability, and detailed analysis of ARCs collectively contribute to the superiority of our approach compared to 1D simulators like SCAPS.

For calibration, we have used the physical structure design of the ATHENA silicon solar cell module regarding the standard integrated Si-wafer processing technology while for the electrical and optical properties for top and bottom cells and also to describe a two-dimensional structure for the top perovskite cell, ATLAS module is used. A top cell is illuminated by AM1.5G, according to its energy gap two ranges are absorbed ultraviolet and visible ranges. Under the top cell, a bottom Si PERL cell is illuminated by a filtered spectrum with a NIR range. Figure 1, shows a device structure [33]. The key parameters of top and bottom layers are summarized in Table 1 [35–42].

3 Results and Discussion

By applying appropriate geometrical and physical parameters for simulator validation, the two standalone sub-cells are calibrated against experiments [33]. For the top cell simulation, an 8 nm of CuSCN layer thickness is deposited on an active perovskite 650 nm layer on a 50 nm and 30 nm for dual ETLs ($PC_{60}BM$-AZO) respectively using an ATLAS module. For the bottom cell simulation, the same order of process steps, as done by William et al. [43], is carried out. The structure simulation is based on an Athena module as follows. A p-type 450 µm thick < 100 > wafer structure is used to study the behavior of optical absorption in which the substrate boron doping concentration is $10^{17}/cm^3$ with 10 µs lifetime. A rear local diffusion of phosphorus is completed at 840 °C for 30 min. A 10 µm base width of inverted pyramids texture surface is realized by etching process. A dual layer of ARC is deposited on the top of it, to reduce reflection with thickness of 25 nm each. A front surface boron diffusion for 60 min at 925 °C has been followed. Before top and bottom passivation and contact definition, a drive-in is done for 60 min at 1050 °C [43].

Then, to obtain the J-V characteristic curves, AM1.5G spectrum is implemented to illuminate the structure. Figure 2a, b and c displays the top and bottom bare and filtered cells comparison of J-V characteristic curves calibration among simulation and measurements, while Fig. 2d exhibits the EQE curves for experimental and simulated cells.

Table 1 Main parameters of the $CH_3NH_3PbI_3$ and c-Si PV cell materials

Parameters	Top Cell				Bottom Cell
Material	CuSCN	$CH_3NH_3PbI_3$	$PC_{60}BM$	ZnO:Al	P-Si
Thickness (μm)	0.008	0.650	0.05	0.03	450
Energy gap (eV)	3.6 [35]	1.7	2 [40]	3.3 [41]	1.12 [42]
Electron affinity (eV)	1.7 [35]	3.9 [36]	3.9 [40]	4.6 [41]	4.05 [42]
Relative permittivity	10 [35]	18 [37]	3.9 [40]	9 [41]	11.9 [42]
Electron mobility (cm^2 /Vs)	100 [35]	3 [38]	0.2 [40]	100 [41]	1.5×10^3[42]
Hole mobility (cm^2 /Vs)	25 [35]	17 [38]	0.2 [40]	25 [41]	4.5×10^2 [42]
CB effective DOS (cm^{-3})	2.2×10^{19} [35]	2.2×10^{18} [39]	2.5×10^{21}[40]	2.2×10^{18}[41]	2.8×10^{19} [42]
VB effective DOS (cm^{-3})	1.8×10^{18} [35]	1.8×10^{19} [39]	2.5×10^{21}[40]	1.8×10^{19}[41]	1.04×10^{19} [42]
Donor concentration N_D (cm^{-3})	_	_	10^{19}	10^{19}	_
Acceptor concentration N_A (cm^{-3})	4×10^{18}	_	_	_	10^{17}

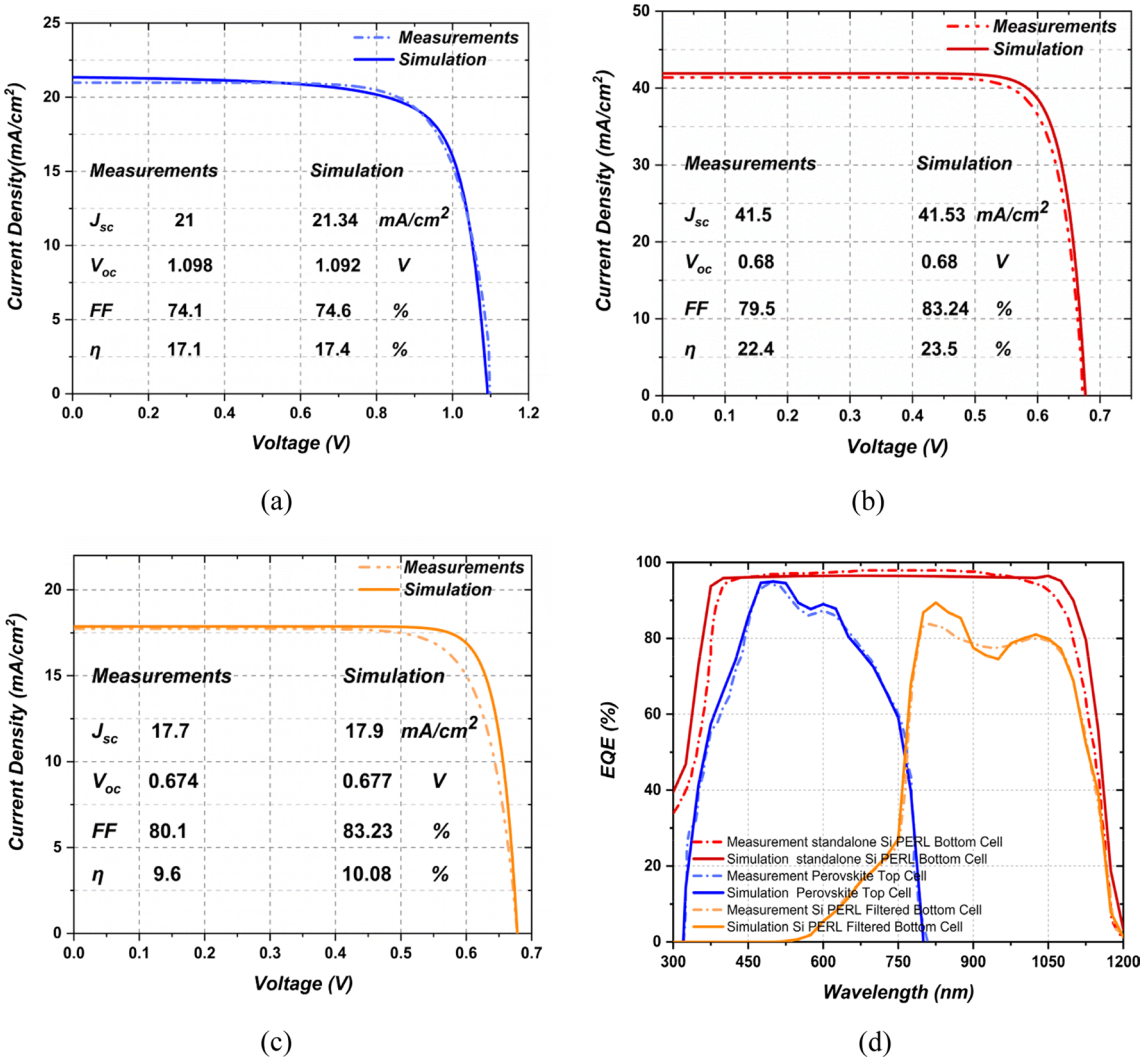

Fig. 2 Comparison of J-V characteristic curves results due to the calibration of Perovskite/PERL tandem cell (**a**) top cell, **b** bare bottom cell and (**c**) filtered bottom cell, **d** EQE curves of both experimental and simulated cells

3.1 Simulation and Optimization of Bifacial Textured 4-T Perovskite/Perl p-Si Tandem

3.1.1 Top Cell Optimization

The photovoltaic working mechanism depends on the design and configuration of the PV cell. Structure optimization is the main road for efficient separation and collection of the photo-excited carriers. To improve the performance of a photovoltaic device, some design-related parameters are to be adjusted:(a) conduction and valence band offsets at the interface (CBO and VBO), (b) Built-in electric field, (c) Effective force field (work function difference, Ohmic and Schottky contact) [44, 45]. The heterojunction interface is a key determinant of voltage, current flow, and electric field on both sides of the junction [44, 45].

a Band Alignment

The ease of flow of photogenerated carriers from the absorber layer to the corresponding electrodes is crucial to cell performance. Thus, selection of appropriate ETLs and HTLs plays a decisive role in improving the performance of the perovskite cell [46].

Notably, the CBO at the interface between the ETL and the absorber and the VBO between the HTL and the absorber show a significant role in cell efficiency. Both of them depend on the electron affinity. So, electron affinity of the ETL and HTL all play a role [45]. The CBO and the VBO are defined as given in the following equations,

$$\mathrm{CBO} = \chi_{\mathrm{Perovskite}} - \chi_{\mathrm{ETL}} \tag{1}$$

$$\mathrm{VBO} = \left(\mathrm{E_g} + \chi\right)_{\mathrm{HTL}} - \left(\mathrm{E_g} + \chi\right)_{\mathrm{Perovskite}} \tag{2}$$

where, E_g is the bandgap and χ is electron affinity.

To demonstrate such effects, we simulated four devices regarding the perovskite-based top cell. First, for the calibrated model with the direct structure (p-i-n) ITO/CuSCN/$CH_3NH_3PbI_3$/PC60PM/AZO/AgNW, Copper (I) thiocyanate (CuSCN) is used as an HTL and PC60BM/AZO as dual ETLs. Figure 3a shows the band diagram for the device. As can be depicted from the figure, there is a small spike at the interface between its dual ETLs which makes some trouble for the electrons to move from first ETL to the second one. Figure 3b exhibits the band diagram for the second simulated structure ITO/CuSCN/$CH_3NH_3PbI_3$/PC60PM/AgNW. The spike-like band disappears, and now it is easy to move the electrons without any obstacles. As a result, efficiency increases from 17.4% to 17.52%. To have a wider view of the optimum CBO for this device, different values of CBOs for various ETLs are tested. $Zn(O_{0.3},S_{0.7})$, C_{60}, TiO_2, ZnO, and CdSe replaced the $PC_{60}BM$ sequentially, each at a time, one after the other. The ETLs material properties used are acquired from [45–48] and [49] and summed up in Table 2. The material that achieves the maximum PCE among the different ETLs analyzed is $Zn(O_{0.3},S_{0.7})$. It was observed that the highest efficiency occurs when the CBO is equal to 0.3 eV. This clearly improves the flow of electrons giving an efficiency of 18.37% (Table 3).

Further, for appropriate HTL design, its valence band maximum (VBM) should be higher than that of the perovskite and to have high hole mobility to extract holes efficiently from the perovskite material [50]. The difference in energy level at HTL/perovskite interface is the VBO [44]. In the third simulated structure ITO/CuSCN/$CH_3NH_3PbI_3$/$Zn(O_{0.3},S_{0.7})$/AgNW, Copper (I) thiocyanate(CuSCN) is exploited as a hole transparent layer. It combines its intrinsic hole-transparency (p-type) characteristics with optical transparency across the visible-to-near-infrared portion of the illumination spectrum due to its large bandgap (~3.6 eV) [51, 52]. However, the existence of compensating donor states, performing as hole traps or scattering centers [53, 54], drastically disrupts the hole transportation mechanism in p-type CuSCN. So, it is desirable to test other alternatives.

As observed in Fig. 3c, the holes accumulate and provide the opportunity for recombination to occur. Band-bending poses rather impediment to the flow of holes and their extraction, thus, prompting search for better materials owing to the significance of HTL, as well as ETL, to cell efficiency. Different HTLs are tested [55], CuI, Nio, MoO_3, Cu_2O, and CZTS replaced the CuSCN sequentially, each at a time, one after the other. The HTLs material properties are summed up in Table 4. After testing different values of VBOs for various HTLs, Copper iodide (CuI) is chosen as a suitable HTL as it yields the highest cell efficiency with VBO = -0.5 eV. It is among those HTLs of p-type copper-based inorganic semiconductors that have high chemical stability, hole mobility and conductivity [56–59] with high abundance and low cost as its most important features. Figure 3d shows a band diagram for the fourth device ITO/CuI/$CH_3NH_3PbI_3$/$Zn(O_{0.3},S_{0.7})$/AgNW. These improvements for a device raise the efficiency up to 19.81% (Table 5). Figures 4a and b show the distinctive values of CBO and VBO for various ETLs and HTLs respectively.

b Electric Field

Electric fields at any interface play a focal role in the operation of PSCs [45, 50]. The electric field of the first simulated cell is illustrated in Fig. 5a. A small peak of negative field is observed at the perovskite/$PC_{60}BM$ interface directed from the $PC_{60}BM$ to the perovskite and a much smaller one from the perovskite to the CuSCN. A positive field rises significantly at the $PC_{60}BM$ /AZO interface from the $PC_{60}BM$ to AZO, but a more prominent

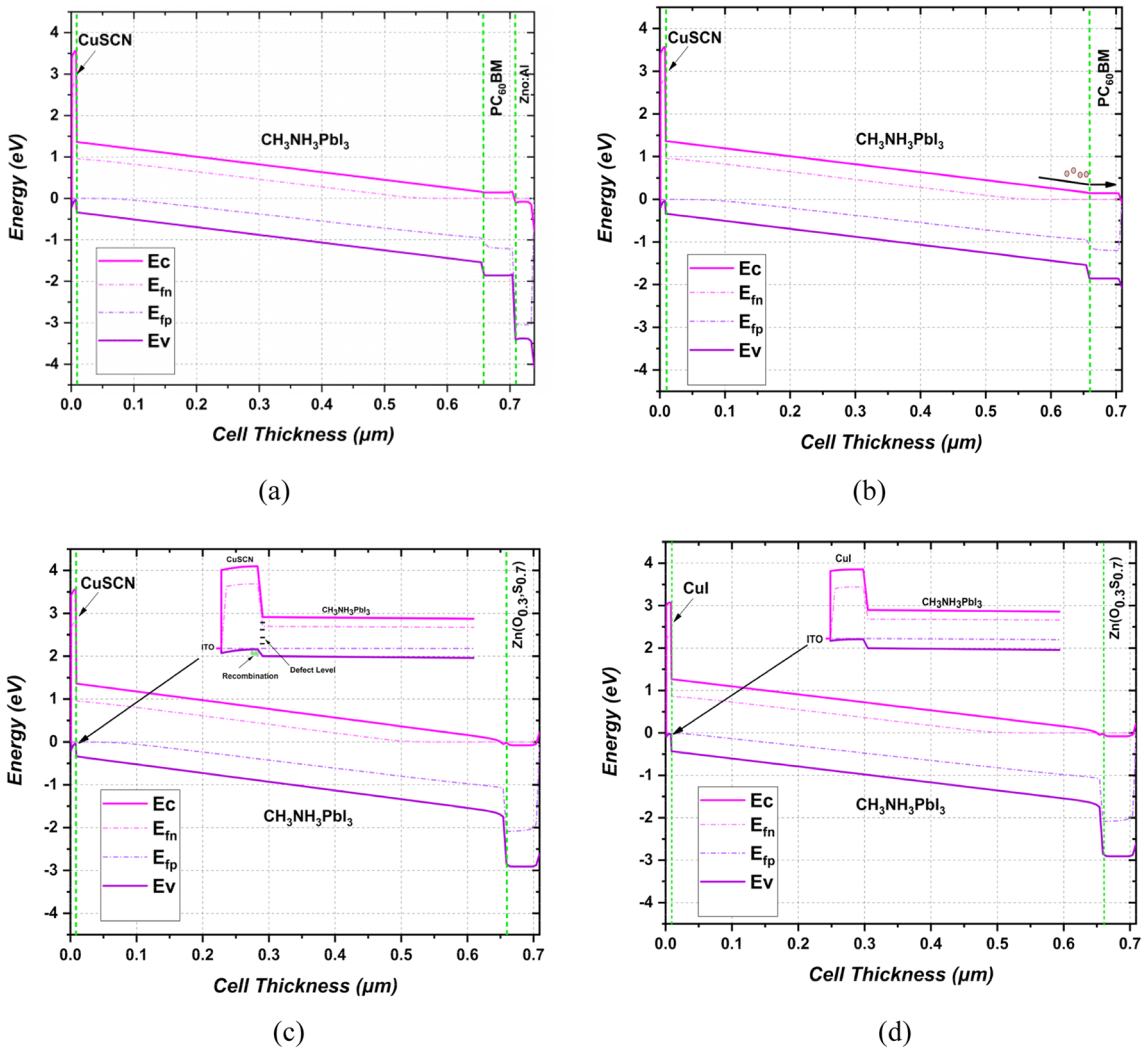

Fig. 3 **a** Energy band diagram of CuSCN/Perovskite/$PC_{60}BM$/AZO/AgNW, **b** Energy band diagram of CuSCN/Perovskite/$PC_{60}BM$/AgNW, **c** Energy band diagram of CuSCN/Perovskite/$Zn(O_{0.3},S_{0.7})$/AgNW, **d** Energy band diagram of CuI/Perovskite/$Zn(O_{0.3},S_{0.7})$/AgNW

Table 2 Material characteristics for different ETLs

Parameters	$Zn(O_{0.3},S_{0.7})$	C_{60}	TiO2	$PC_{60}BM$	ZnO	CdSe
Energy gap (eV)	2.83	1.7	3.2	2	3.3	2.16
Electron affinity (eV)	3.6	3.9	4	3.9	4.1	4.3
Relative permittivity	9	4.2	9	3.9	9	10.6
Electron mobility (cm^2 /Vs)	100	8×10^{-2}	20	0.2	100	100
Hole mobility (cm^2 /Vs)	25	3.5×10^{-3}	10	0.2	50	50
CB effective DOS (cm^{-3})	2.2×10^{18}	8×10^{19}	2.1×10^{18}	2.5×10^{21}	4×10^{18}	2.2×10^{18}
VB effective DOS (cm^{-3})	1.8×10^{19}	8×10^{19}	1.8×10^{19}	2.5×10^{21}	1×10^{19}	1.8×10^{19}

Table 3 Comparison of the Electrical parameters for various ETLs

Parameters	CdSe	$PC_{60}BM$	ZnO	C_{60}	TiO_2	$Zn(O_{0.3},S_{0.7})$
J_{sc} (mA/cm^2)	21.38	21.34	21.34	21.47	21.37	21.37
V_{oc} (V)	1.05	1.09	1.09	1.10	1.10	1.10
FF (%)	65.82	74.6	75.10	76.71	77.09	77.7
η (%)	14.85	17.4	17.49	18.12	18.16	18.37

Table 4 Material characteristics for different HTLs

Parameters	CuI	NiO	MoO_3	CuSCN	Cu_2O	CZTS
Energy gap (eV)	3	3.8	3	3.6	2.27	1.2
Electron affinity (eV)	2.1	1.46	2.3	1.7	3.2	4.1
Relative permittivity	6.5	10.7	12.5	10	7.11	7
Electron mobility (cm^2 /Vs)	100	12	25	100	200	25
Hole mobility (cm^2 /Vs)	44	2.8	100	25	80	20
CB effective DOS (cm^{-3})	2.8×10^{19}	2.8×10^{19}	2.2×10^{18}	2.2×10^{19}	2.2×10^{18}	2×10^{19}
VB effective DOS (cm^{-3})	1×10^{19}	1×10^{19}	1.8×10^{19}	1.8×10^{18}	1.9×10^{19}	1.8×10^{19}

Table 5 Comparison of the Electrical parameters for various HTLs

Parameters	CZTS	Cu_2oO	CuSCN	MoO_3	NiO	CuI
J_{sc} (mA/cm^2)	18.28	20.49	21.37	21.34	21.37	21.39
V_{oc} (V)	1.02	1.10	1.10	1.14	1.14	1.16
FF (%)	66.56	75.70	77.7	77.51	77.85	79.7
η (%)	12.46	17.14	18.37	18.92	19.10	19.81

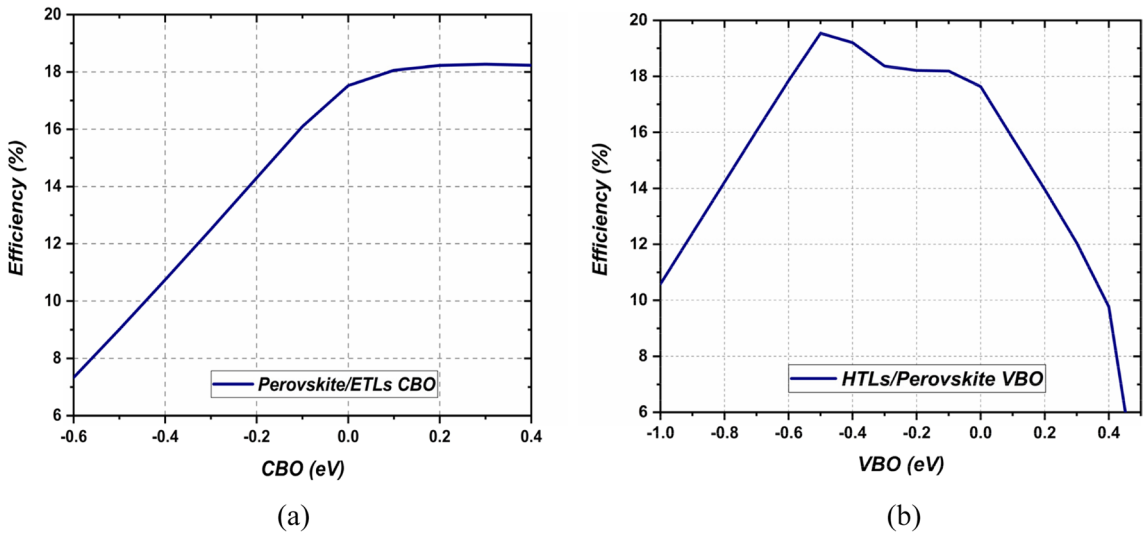

Fig. 4 **a** CBO curve for Perovskite/ETLs, **b**VBO curve for HTLs /Perovskite

negative field at the AZO /Electrode interface from electrode to AZO. When the perovskite material absorbs light, the generated electron–hole pairs are split by appropriate electric fields [50]. At Perovskite/ $PC_{60}BM$ interface, the negative electric field pushes the electron to move toward $PC_{60}BM$. This flow of electrons, to some extent, is hindered by the positive electric field at the $PC_{60}BM$/AZO interface which consequently increases recombination rate in this region for the electrons moving from the $PC_{60}BM$ to the AZO. One the other hand, the negative electric field at the AZO/AgNW interface helps decrease the electron recombination loss for those proceeding from the AZO to the contact. In the same manner, the positive electric field near ITO/CuSCN increases the recombination loss at their common interface, while at the CuSCN/Perovskite interface, the negative electric field boasts the transfer of holes to the CuSCN. There is no positive electric field that may impede the movement of the electrons at the ETLs interface, the electric field between PC60BM and AgNW is negative so the electron can move easily towards AgNW (Fig. 5b) for a second simulated device. A -5×10^5 V/cm is a negative electric field strength at the Perovskite/ETL interface when $Zn(O_{0.3},S_{0.7})$ is used in the third simulated cell, so the electrons now can move easily, therefore, the efficiency increased (Fig. 5c). As a result of adding CuI in the fourth device, the positive electric field strength at the ITO/CuI decreases, partly easing the movement of holes (Fig. 5d).

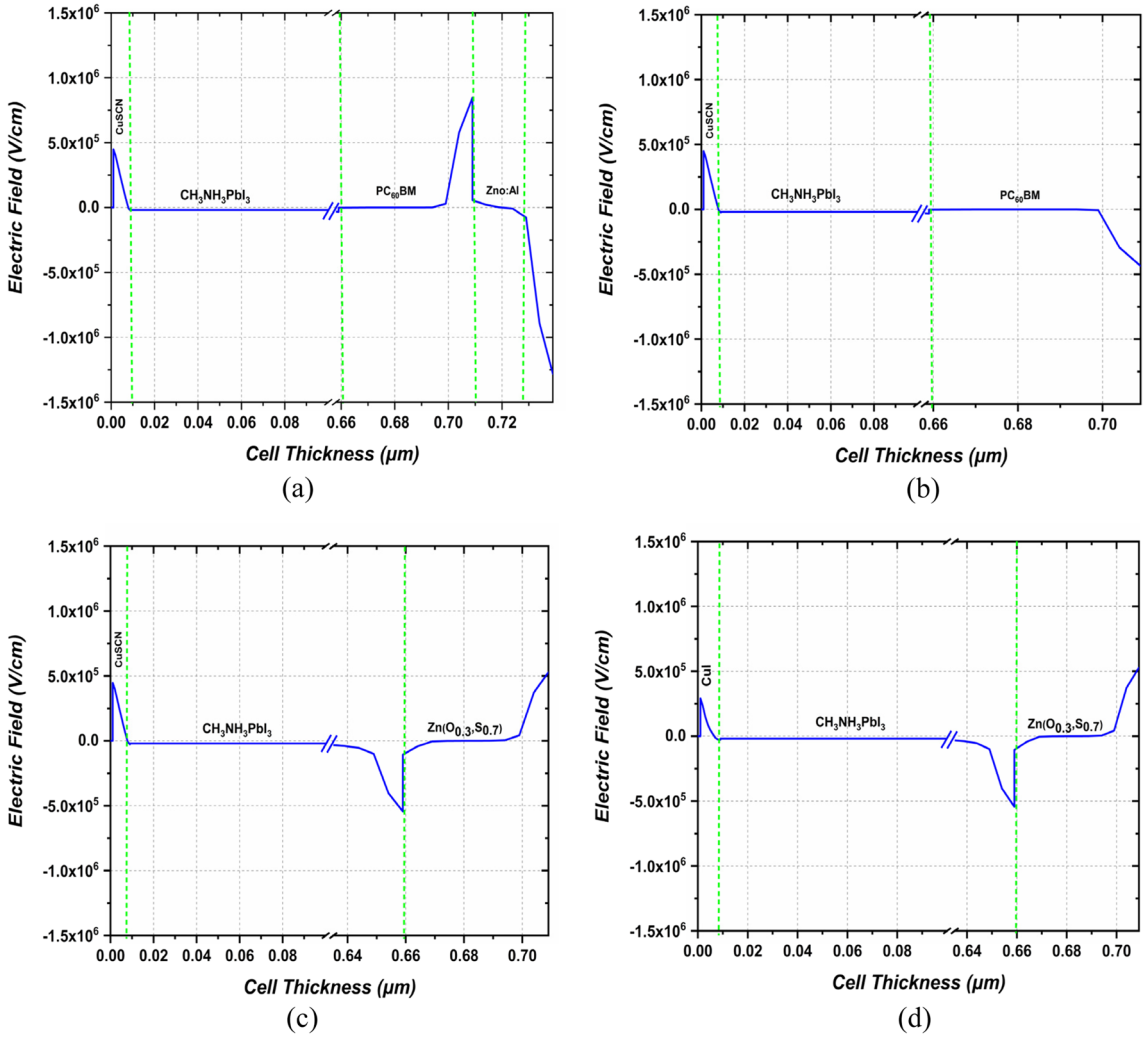

Fig. 5 Electric field for different structures, **a** ITO/CuSCN/Perovskite/$PC_{60}BM$/AZO/AgNW, **b** ITO/CuSCN/Perovskite/$PC_{60}BM$/AgNW, **c** ITO/CuSCN/Perovskite/$Zn(O_{0.3}S_{0.7})$/AgNW and **d** ITO/CuI/Perovskite/$Zn(O_{0.3}S_{0.7})$/AgNW

iii. Ohmic and Schottky contact

As shown in Fig. 3c, a Schottky barrier, rather than an ohmic contact, is obtained between ITO/CuSCN due to the disparity between their work functions. This eventually results in band-bending in the p-type semiconductor representing the creation of electric field through diffusion of charge carriers toward the side of larger work function of the semiconductor in comparison to that of the metal contact. Proliferation of mobile charges in the metal contact prevent bending of its band for their ability to easily react to the created field [60]. As a result of adding CuI, the Schottky barrier between ITO/CuI also decreases as shown in Fig. 3d.

Also, charge recombination profiles of PSCs yield a deeper insight into their physics and operation mechanisms. Figure 6 shows the recombination rates of the simulated PV cells under discussion. In Fig. 6a, AZO has the highest recombination rate in the order of $\sim 5 \times 10^{20}$ cm^{-3} s^{-1}. The electron recombination rate from the $PC_{60}BM$ to the AZO also increases because of the positive electric field at their common interface (10^{20} cm^{-3} s^{-1}). Then, it goes back down to 5×10^{19} at the AZO/AgNW interface as a result of the negative field at this interface. After removing a AZO layer, the recombination rate between ETL (PC60BM) and AgNW decreases to $\sim 4 \times 10^{17}$ cm^{-3} s^{-1} (Fig. 6b). 1×10^{13} cm^{-3} s^{-1} is a recombination rate inside the $Zn(O_{0.3}, S_{0.7})$ layer after using it instead of PC60BM and $\sim 1 \times 10^{-35}$ cm^{-3} s^{-1} at the $Zn(O_{0.3}, S_{0.7})$/AgNW interface (Fig. 6c). The recombination rate at the HTL/Perovskite decreases from 10^{20} cm^{-3} s^{-1} to $\sim 6 \times 10^{19}$ cm^{-3} s^{-1} when CuI is also used instead of CuSCN (Fig. 6d). Figure 7a illustrates the EQE curves for different structures, while Fig. 7b shows a comparison between current densities in different structures for top cell. The EQE of the different design cases are nearly the

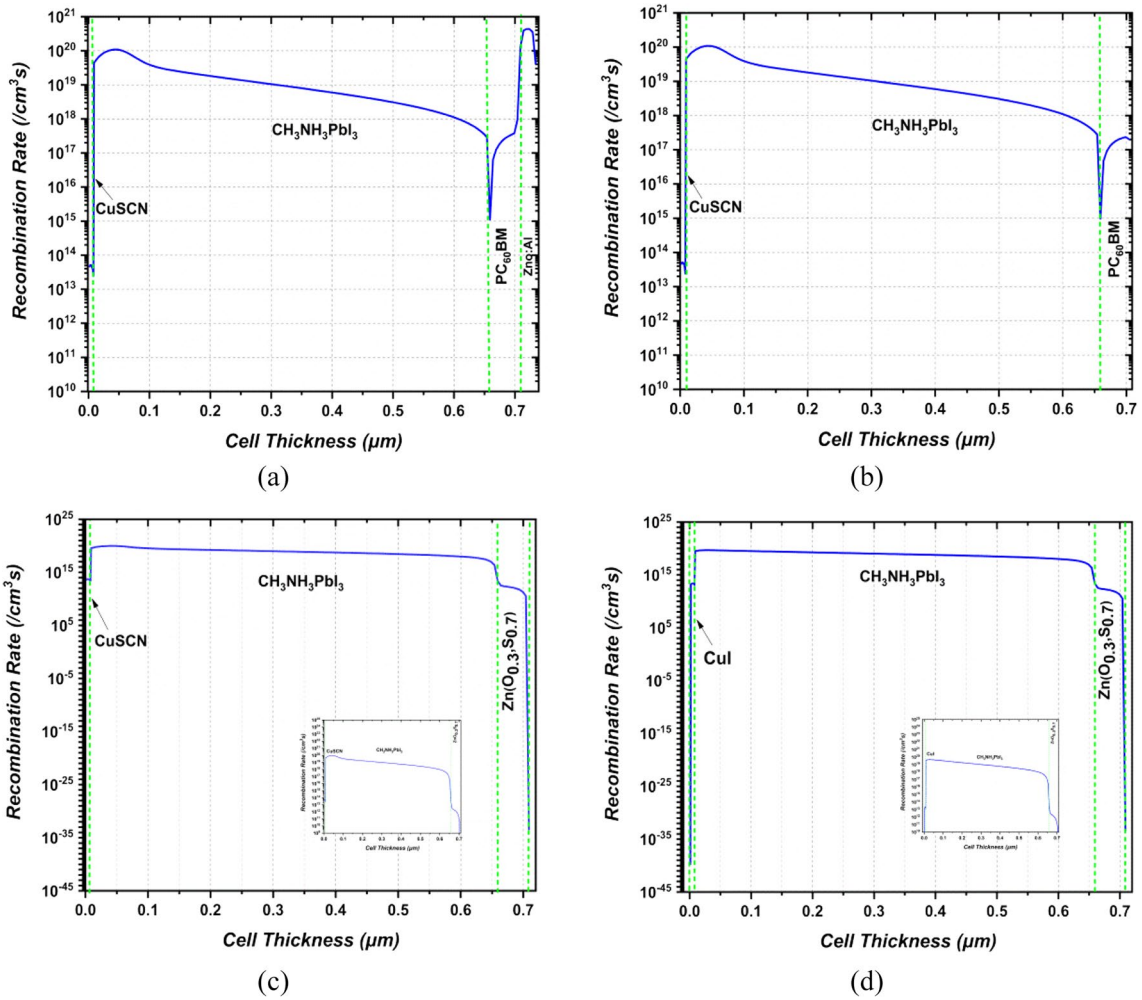

Fig. 6 Charge recombination for different structures, **a** ITO/CuSCN/Perovskite/$PC_{60}BM$/AZO/AgNW, **b** ITO/CuSCN/Perovskite/$PC_{60}BM$/AgNW, **c** ITO/CuSCN/Perovskite/$Zn(O_{0.3},S_{0.7})$/AgNW, **d** ITO/CuI/Perovskite/$Zn(O_{0.3},S_{0.7})$/AgNW

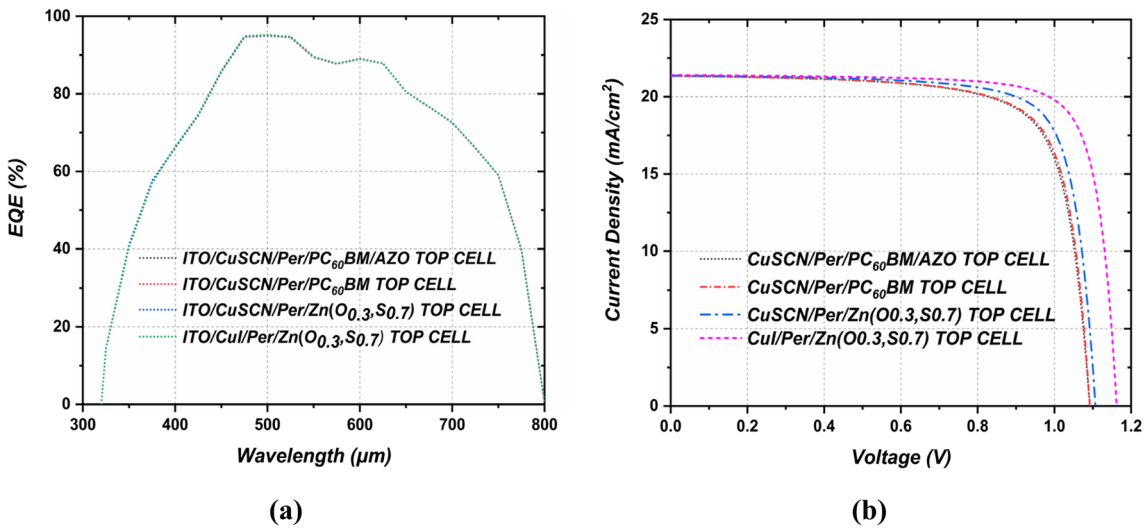

Fig. 7 **a** EQE for various structures and (**b**) Comparison between current densities in different structures for Top Cell

Table 6 Shows a comparison between four devices for Top Cell

Structure	J_{sc} (mA/cm^2)	V_{oc} (V)	FF (%)	η (%)
ITO/CuSCN/Perovskite/$PC_{60}BM$/AZO/AgNW	21.34	1.092	74.6	17.4
ITO/CuSCN/Perovskite/$PC_{60}BM$/AgNW	21.34	1.092	75.18	17.52
ITO/CuSCN/Perovskite/$Zn(O_{0.3},S_{0.7})$/AgNW	21.37	1.106	77.7	18.37
ITO/CuI/Perovskite/$Zn(O_{0.3},S_{0.7})$/AgNW	21.39	1.162	79.7	19.81

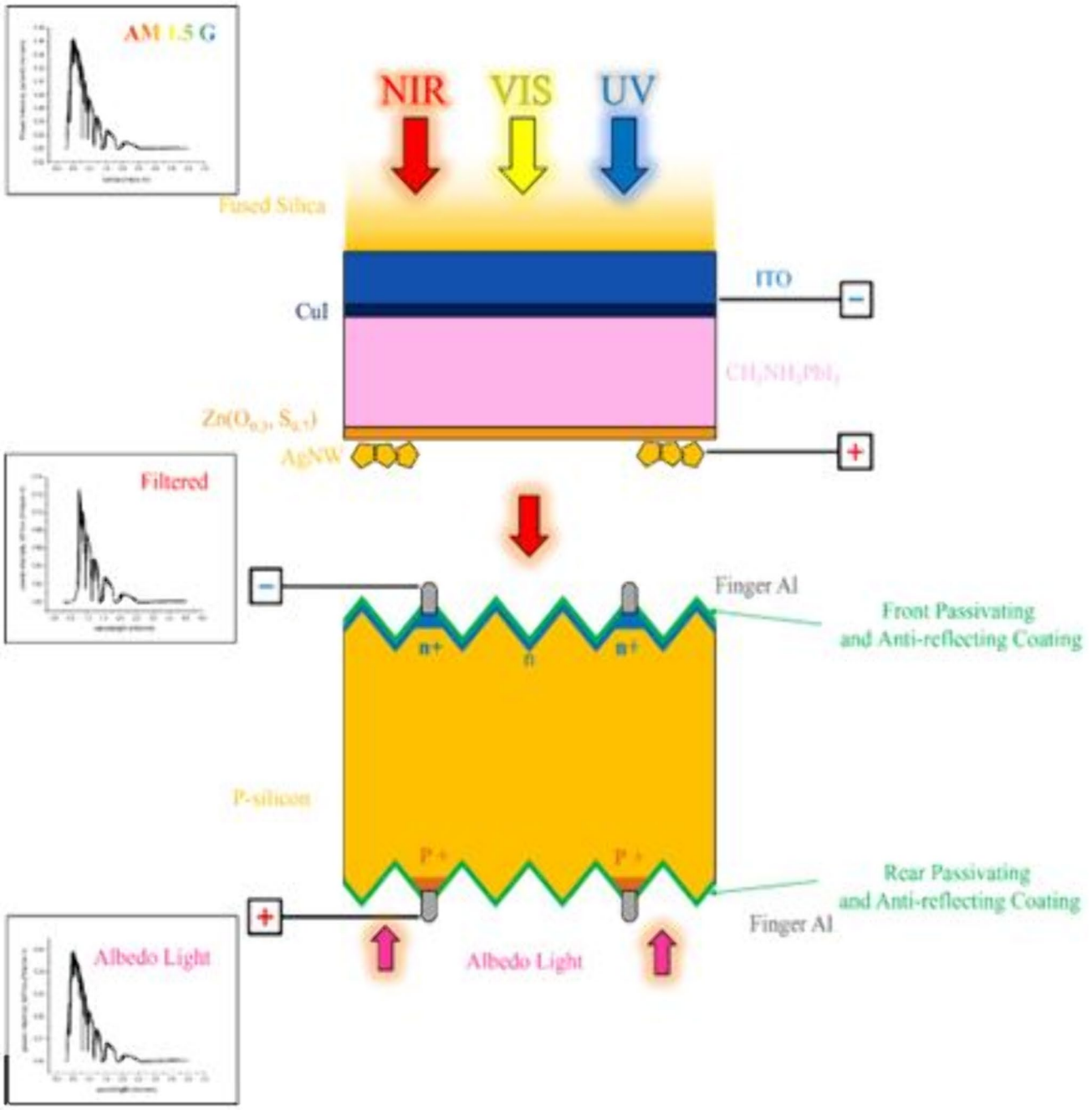

Fig. 8 The schematic diagram of a new 4-T tandem

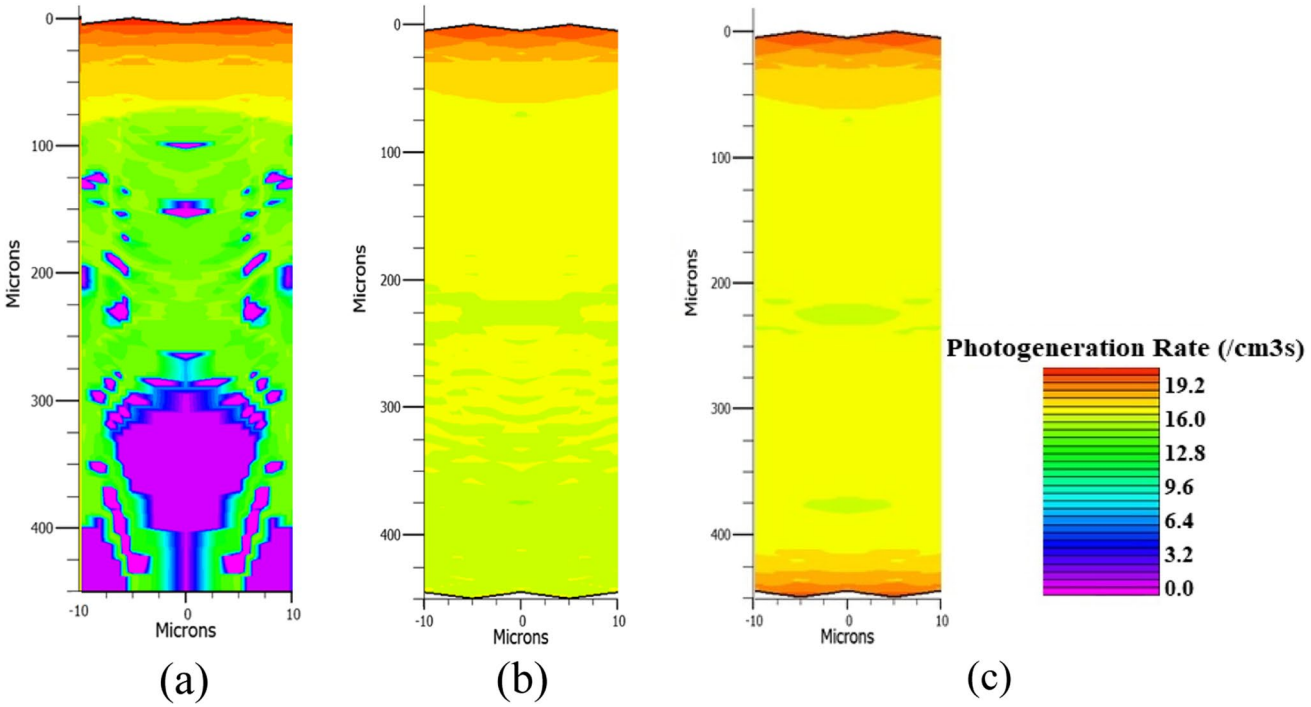

Fig. 9 Photo-generation profile for (**a**) Calibrated, **b** Mono-facial dual-texture at lifetime (1000 µs), **c** Bifacial dual- texture for bare Si bottom cell at 1000 µs

same, signifying a constant short circuit current as indicated in Fig. 7b. Further, Table 6 shows the steps of upper cell optimization.

3.1.2 Bottom Cell Optimization

Notably, 30% of the reflection occurs on the bare silicon surface. The reflection loss on cell surface is a severe problem. It is one of the causes that lead to the deterioration of the PCE of the crystalline silicon solar cell [61]. Two of the prime candidate approaches for a light trapping structure are used for minimizing reflection: 1) texture treatment and 2) adding ARC to the surface [62]. Another light trapping technique has been proposed, which is a back-surface treatment for an anti-irregular reflection

Table 7 Simulated Output Parameters of Mono-facial dual-sided texture Perl Si bottom solar cell

Perl Si Cell	Lifetime µs	J_{sc}(mA/cm^2)	V_{oc}(V)	FF (%)	η (%)
Bare	10	43.04	0.68	82.54	24.13
	100	44.20	0.70	83.77	25.91
	1000	44.68	0.72	84.42	27.15
Filtered	10	18.53	0.679	82.32	10.35
	100	20.54	0.709	83.95	12.22
	1000	21.24	0.723	84.79	13.02

[61]. Figure 8 shows the schematic diagram of a new 4-T tandem investigated in this work. Although reflection of incident light can be reduced by front-side surface texture and ARC films, light can escape from the cell resulting in optical losses [63, 64]. As exhibited in Fig. 9a, the raytracing for calibration device shows that there are some areas in a Si bulk where light has not reached at all. This makes electron–hole pair production in them non-existent, meaning that the photo-generation rate is equal zero (Dark purple areas), which leads to reduced efficiency. A textured front surface with a planar rear surface is a basic structure for common high-efficiency silicon solar cells [65–67]. Recently theoretical simulations involving double-sided texture have been proven to augment spectrum absorption in Si cells [68, 69]. For the current device simulation, getting better results for Perl p-Si bottom cell efficiency is through enhancing carriers photo-generation by optimizing optical absorption, where 10 µm base size of inverted pyramids of texture rear surface is realized by etching process then adding dual ARC films. After double-sided pyramidal texture, Silicon solar cell is capable of superior light trapping than PV devices with texture on just the front as shown in Fig. 9b. The raytracing shows that all regions are now capable of producing photo-current after many reflections for light on rear textured side surface, the dark purple areas all disappeared. The J-V characteristics for different lifetimes 10, 100 and 1000 µs for the device

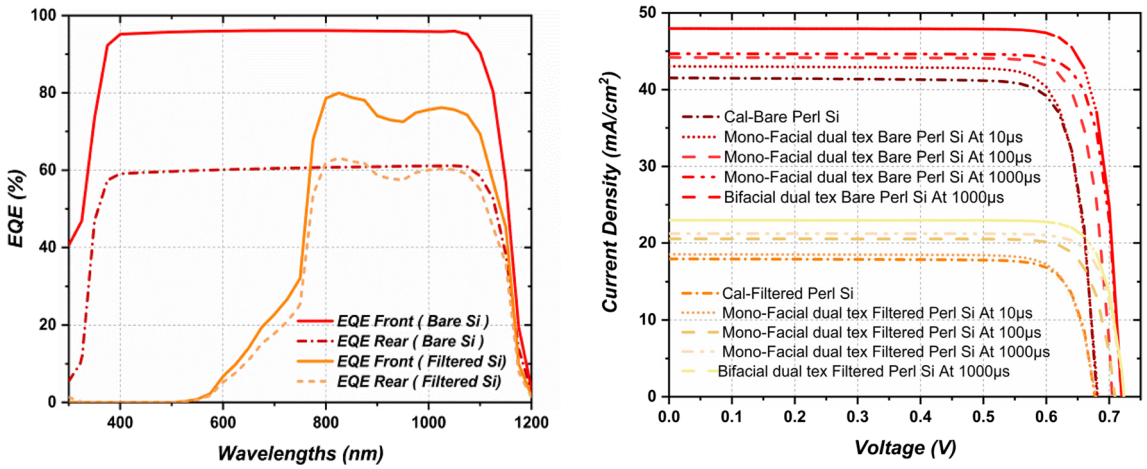

(a) (b)

Fig. 10 **a** EQE for bifacial bare and filtered Perl Si cells, **b** Currents for Mono and Bifacial Bare and Filtered Perl Si cell

Table 8 Comparison between calibrated, mono-facial dual-sided texture and bifacial dual-sided texture

Type	Bottom Cell	J_{sc}(mA/cm^2)	V_{oc}(V)	FF (%)	η (%)
Calibrated	**Bare**	41.53	0.68	83.24	23.5
	Filtered	17.9	0.677	83.23	10.08
Mono-facial dual-sided texture at 1000 µs	**Bare**	44.68	0.72	84.42	27.15
	Filtered	21.24	0.723	84.79	13.02
Bifacial dual-sided texture at 1000 µs	**Bare**	47.9	0.72	84.43	29.11
	Filtered	22.97	0.723	84.79	14.08

are obtained. Table 7 shows the various output electrical parameters for bottom bare and filtered cells at these different lifetimes. As an be inferred, there is a noticeable change in the electrical properties of a current device as the lifetime increases. Efficiencies of 27.15% and 13.02% are shown for 1000 µs lifetime for bare and filtered bottom cells, respectively.

Recently, the PCE of Si cells has become limited [17, 70, 71]. The conversion efficiency of mono-facial PV devices is difficult to enhance [72, 73]. To overcome this and for the production of high-efficiency solar cells, several technologies have been

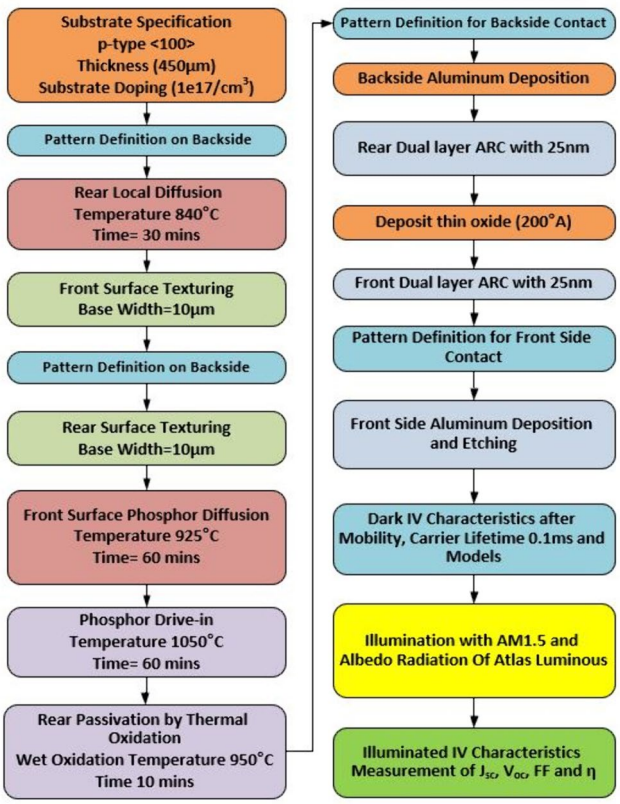

Fig. 11 Flowchart Process design for optimized bottom solar cell simulation

Table 9 Highest reported efficiency regarding 4-T perovskite/si tandems cell with different types of Si bottom cells

Bottom_Si Cell Structure	Semi-transparent perovskite top cell	Configuration	J_{sc} (mA/cm^2)	V_{oc} (V)	FF (%)	Sub-cell η (%)	Tandem η(%)	Year
IBC	$MAPbI_3$	Bare Si	41.3	0.651	75.1	20.2	25.2 [33]	2018
		Filter Si	17	0.633	75.2	8.1		
		Perovskite cell	21	1.098	74.1	17.1		
	$Cs_{0.05}(MA_{0.17}FA_{0.83})_{0.95}Pb(I_{0.9}Br_{0.1})_3$	Bare Si	40.7	0.728	80.3	23.8	26.3 [79]	2018
		Filter Si	17.7	0.705	80	10		
		Perovskite cell	19.4	1.075	78.1	16.3		
	$Cs_{0.15}(FA)_{0.85}Pb(I_{0.7}1Br_{0.29})_3$	Bare Si	41.3	0.691	80.6	23.8	27.1 [80]	2019
		Filter Si	24.1	0.678	81.2	13.3		
		Perovskite cell	15.4	1.22	73.4	13.8		
SHJ	$MAPbI_3$	Bare Si	41.1	0.708	80.3	23.3	27 [81]	2019
		Filter Si	15.6	0.698	80.1	8.7		
		Perovskite cell	19.8	1.156	79.9	18.3		
IBC	$Rb_{0.05}Cs_{0.095}MA_{0.1425}FA_{0.7125}PbI_2Br$	Bare Si	42.5	0.717	81	24.7	27.8 [82]	2020
		Filter Si	19.6	0.697	78	10.7		
		Perovskite cell	18	1.205	78.9	17.1		
PERL		Bare Si	40.1	0.699	80.1	22.4	26.2 [82]	
		Filter Si	18.6	0.675	80.4	10.1		
		Perovskite cell	17.5	1.205	76.3	16.1		
POLO-IBC	$FACsPbI_{3-x}Br_x$	Bare Si	41.4	0.69	81.2	23.2	26.2 [83]	2020
		Filter Si	15.6	0.66	80.2	8.2		
		Perovskite cell	19.7	1.16	78.7	18		
Single side n-TOP Con	$Cs_{0.05}FA_{0.8}MA_{0.15}PbI_{2.55}Br_{0.45}$	Bare Si	39.2	0.702	80.1	22	26.7 [84]	2020
		Filter Si	16.6	0.675	79.6	8.9		
		Perovskite cell	20.5	1.11	78.6	17.9		
SHJ	$CsFAPbI_{3-x}$	Bare Si	40.1	0.708	82.5	23.4	28.3 [85]	2021
		Filter Si	14.5	0.69	83	8.5		
		Perovskite cell	21.9	1.13	79.7	19.8		
	$Cs_xFA_{1-x}Pb(I_yBr_zCl_{1-y-z})_3$	Bare Si	39.87	0.74	83.17	24.53	30.24 [86]	2022
		Filter Si	19.56	0.72	82.89	11.67		
		Perovskite cell	18.82	1.24	79.58	18.57		
	$Cs_x(FA_{0.4}MA_{0.6})_{1-x}PbI_{2.8}Br_{0.2}$	Bare Si	38.68	0.72	78.61	22.14	28.38 [87]	2023
		Filter Si	12.29	0.69	82.5	7.07		
		Perovskite cell	23.11	1.14	80.52	21.31		
SST poly-SiO_x	perovskite	Bare Si	38.68	0.695	80.33	20.47	27.97 [88]	2023
		Filter Si	16	0.666	77.6	8.27		
		Perovskite cell	22	1.139	78.6	19.7		
DST poly-SiO_x	perovskite	Bare Si	37.85	0.655	78.42	19.44	28.07 [88]	2023
		Filter Si	16.8	0.637	78.2	8.37		
		Perovskite cell	22	1.139	78.6	19.7		
C-Si	perovskite	Bare Si	34.81	0.68	83.60	19.83	35.43 [89]	2024
		Filter Si	32.47	0.67	83.50	19.74		
		Perovskite cell	15.47	1.37	73.49	15.69		
		Bare Si	0.68	34.81	83.60	19.83	25.86 [89]	2024
		Filter Si	17.77	0.73	83.72	16.29		
		Perovskite cell	15.86	0.8	74.69	9.57		
PERL	$CH_3NH_3PbI_3$	Bare Si	44.68	0.72	84.42	27.15	32.83	
		Filter Si	21.24	0.723	84.79	13.02	**Without albedo**	
		Perovskite cell	21.39	1.162	79.7	19.81		
		Bare Si	47.9	0.72	84.43	29.11	33.89	
		Filter Si	22.97	0.723	84.79	14.08	**With albedo**	
		Perovskite cell	21.39	1.162	79.7	19.81	Our WORK	

developed that use different concepts and structures to make the most out of the incident light power such as bifacial solar cells. Capturing, absorbing and trapping light inside the solar cell within its boundaries on the front and rear surfaces is the primary goal of bifacial cells. Up to 30% higher yield can be achieved with this type of cells compared to conventional ones when installed outdoors. The effectiveness of both sides of bifacial cells looks similar, with the front side serving as the collection emitter and the back side functioning as the back-surface-field (BSF). Using bifacial has been shown for decades but has only recently received widespread attention [74]. Bifacial solar cells are aimed at harnessing light reflected from surrounding environment, mainly ground surface (Albedo), as well as the normal incident light requiring comprehensive illumination modelling to successfully assess energy outturn [75].

The back contact is designed to have a finger-grid shape allowing light through while the front is kept as those of the conventional devices implemented using screen-printing. Passivated emitter rear contacts (PERC/PERT/PERL) or IBC contacting scheme upgraded technologies contrived this type of devices prospecting around 60% of market dominance by 2029 [76–78]. The simulation of the proposed bifacial 4-T tandem is performed under AM1.5G with 90° at the front surface and albedo (~30%) at 270° for the rear side of the tandem. This leads to an improvement in the electrical properties of the Perl Si cell. Figure 9c, shows a bifacial dual-texture for the bare Si bottom cell for 1000 µs, the photo-generation rate at the rear textured side surface increases and other areas according to albedo.

The EQE now for bifacial dual-texture for bare Si bottom cell is divided into two parts, a special part for a front textured surface side and the other for a rear textured surface side (see Fig. 10a). Table 8 shows a comparison between bare and filtered Perl Si cells at different lifetimes. It is found that the efficiency increases by 1.96% over the last optimization for the bare cell and 1.06% for the filtered. Figure 10b shows all currents for Mono and Bifacial Bare and Filtered Perl Si cells.

As a result, the total PCE of the proposed bifacial textured 4-T Perovskite/Perl p-Si tandem solar cell reaches 33.89%, when optimized semitransparent PSC (19.81%) is mechanically stacked upon an optimized PERL p-silicon solar cell (14.08%). The flowchart in Fig. 11 shows the steps of the process and electrical simulations of the optimized device. Table 9 shows a survey for 4-T perovskite/Si tandems from 2018 up to 2024.

4 Conclusions

In this study, we introduced a TCAD model structure of a 4-terminal (4-T) Perovskite/PERL silicon (Si) tandem solar cell. In order to ensure the accuracy of our simulation model, the calibration of the two standalone sub-cells was performed using experimental data. Our simulations explored four different structures for the top perovskite cell, yielding the following findings. The initial structure comprises ITO/CuSCN/Perovskite/PC60PM/AZO/AgNW. An efficiency of 17.4% has been achieved. The issue related to this structure is that a small spike in the energy band diagram at the interface between the two ETLs impeded electron movement. To alleviate this problem, the second structure (ITO/CuSCN/Perovskite/PC60PM/AgNW) is proposed, in which AZO was removed and PC60PM was used as the sole ETL. This modification slightly improved efficiency to 17.52% by addressing the energy band spike. The third structure consists of the stacked layers ITO/CuSCN/Perovskite/Zn(O0.3,S0.7)/AgNW. Using Zn(O0.3,S0.7) as the ETL material improved efficiency to 18.37% by optimizing the CBO. In addition to the engineering of the CBO, an additional adjustment for the VBO was carried out, leading to the fourth structure (ITO/CuI/Perovskite/Zn(O0.3,S0.7)/AgNW). In this cell, CuSCN was replaced with CuI as the HTL, resulting in an improved efficiency of 19.81%.

Moreover, for the PERL p-Si bottom cell, we achieved a conversion efficiency of 27.15% for the bare Si cell at a 1000 µs lifetime and 13.02% for the filtered cell. Efficiency improvements were achieved through surface texturing with pyramids and the addition of an ARC. Further optimization involved texturing the rear surface with inverted pyramids. The approach of bifacial dual-side-textured configuration was introduced to maximize the utilization of incident light power, resulting in a bare cell efficiency of 29.11% and a filtered cell efficiency of14.08%. Combining the optimized top and bottom cells, the overall PCE of the 4-T Perovskite/PERL p-Si tandem PV cell proposed in our research reached 33.89%. These simulation results are encouraging and hold significant potential for future experimental exploration, paving the way for more efficient tandem solar cells.

Author Contributions All authors contributed to the study conception and design. Material preparation, data collection and analysis were performed by all authors. The first draft of the manuscript was written by Hend Ahmed. All authors read and approved the final manuscript.

Data Availability No datasets were generated or analysed during the current study.

Declarations This article does not contain any studies involving human participants performed by any of the authors.

The authors declare that no funds, grants, or other support were received during the preparation of this manuscript.

Consent to Participate Not applicable.

Consent for Publication Not applicable.

Competing Interests The authors declare no competing interests.

References

1. Luque A, Hegedus S (2011) Handbook of Photovoltaic Science and Engineering, vol, 2nd edn. Wiley & Sons
2. Orr JC et al (2005) Anthropogenic ocean acidification over the twenty-first century and its impact on calcifying organisms. Nature 437(7059):681–686. https://doi.org/10.1038/nature04095
3. Andersson AJ, Mackenzie FT, Lerman A (2006) Coastal ocean CO2-carbonic acid-carbonate sediment system of the Anthropocene. Global Biogeochem Cycles 20(1):1–13. https://doi.org/10.1029/2005GB002506
4. Karl TR, Trenberth KE (2016) "Modern Global Climate Change," Published by : American Association for the Advancement of Science Stable URL : http://www.jstor.org/stable/3835878 JSTOR is a not-for-profit service that helps scholars, researchers, and students discover, use, and build. 302(5651):1719–1723. https://doi.org/10.1126/science.1090228. Accessed 2 Jan 2024
5. Jacobson MZ, Masters GM (2001) Energy: Exploiting wind versus coal. Science (80-) 293(5534):1438. https://doi.org/10.1126/science.1063376
6. Pacala S, Socolow R (2004) Stabilization wedges: Solving the climate problem for the next 50 years with current technologies. Science (80-) 305(5686):968–972. https://doi.org/10.1126/science.1100103
7. Fthenakis V, Mason JE, Zweibel K (2009) The technical, geographical, and economic feasibility for solar energy to supply the energy needs of the US. Energy Policy 37(2):387–399. https://doi.org/10.1016/j.enpol.2008.08.011
8. Siebentritt S (2021) Photovoltaics the Shockley-Queisser limit 1–24
9. Wang Z, Song Z, Yan Y, Liu S (Frank), Yang D (2019) Perovskite—a Perfect Top Cell for Tandem Devices to Break the S–Q Limit. Adv Sci 6(7). https://doi.org/10.1002/advs.201801704
10. Zuo C, Ding L (2015) Bulk heterojunctions push the photoresponse of perovskite solar cells to 970 nm. J Mater Chem A 3:9063–9066. https://doi.org/10.1039/C4TA04482G
11. De Wolf S et al (2014) Organometallic halide perovskites: Sharp optical absorption edge and its relation to photovoltaic performance. J Phys Chem Lett 5(6):1035–1039. https://doi.org/10.1021/jz500279b
12. Dong Q et al (2015) Electron-Hole diffusion length >175 nm. Sci Express 43210(5760):1–8. https://doi.org/10.1126/science.aaa5760
13. Zuo C, Bolink HJ, Han H, Huang J, Cahen D, Ding L (2016) Advances in perovskite solar cells. Adv Sci 3(7):1–16. https://doi.org/10.1002/advs.201500324
14. Yuan M et al (2016) Perovskite energy funnels for efficient light-emitting diodes. Nat Nanotechnol 11(10):872–877. https://doi.org/10.1038/nnano.2016.110
15. Mcmeekin DP et al (2016) A mixed-cation lead mixed-halide perovskite absorber for tandem s(1).pdf. 351(6269):151–155 [Online]. Available:https://www-herz.physics.ox.ac.uk/publications/McMeekin16a.pdf,10.1126%2Fscience.aad5845. Accessed 5 Dec 2024
16. Yoshikawa K et al (2017) Silicon heterojunction solar cell with interdigitated back contacts for a photoconversion efficiency over 26%. Nat Energy 2(5). https://doi.org/10.1038/nenergy.2017.32
17. Yoshikawa K et al (2017) Exceeding conversion efficiency of 26% by heterojunction interdigitated back contact solar cell with thin film Si technology. Sol Energy Mater Sol Cells 173(April):37–42. https://doi.org/10.1016/j.solmat.2017.06.024
18. Werner J, Niesen B, Ballif C (2018) Perovskite/Silicon Tandem Solar Cells: Marriage of Convenience or True Love Story? – An Overview. Adv Mater Interfaces 5(1):1–19. https://doi.org/10.1002/admi.201700731
19. Taguchi M. 24.7% Record Efficiency HIT Solar Cell on Thin Silicon Wafer. IEEE J Photovolt 4(1). https://doi.org/10.1109/JPHOTOV.2013.2282737
20. Saha P, Singh S, Bhattacharya S (2023) Eco-friendly methylammonium tin-based planar p–n homojunction perovskite solar cells: Design and performance estimation. Int J Mod Phys B 37. https://doi.org/10.1142/S0217979223501692
21. Saha P, Singh S, Bhattacharya S (2023) Higher efficiency and stability in planar homojunction hybrid antimony ($MA_3Sb_2I_9$)- Based perovskite solar cells. IEEE J Quantum Electron 59. https://doi.org/10.1109/JQE.2023.3283521
22. Jianhua Zhao AW (n.d.) Solar Energy Materials and Solar Cells 41:87–99
23. Green MA, Emery K, King DL, Igari S, Warta W (2003) Solar cell efficiency tables (Version 22). Prog Photovoltaics Res Appl 11(5):347–352. https://doi.org/10.1002/pip.499
24. Zhao J, Wang A, Green MA (1999) 24.5% efficiency silicon PERT cells on MCZ substrates and 24.7% efficiency PERL cells on FZ substrates. Prog Photovoltaics Res Appl 7(6):471–474. https://doi.org/10.1002/(SICI)1099-159X(199911/12)7:6%3c471::AID-PIP298%3e3.0.CO;2-7
25. Zhao J (2011) Passivated emitter rear locally diffused solar cells. Bull Adv Technol Res 5(8)
26. Smets A (2016) Solar Energy: The Physics and Engineering of Photovoltaic Conversion, Technologies and Systems. UIT Cambridge
27. Zin N et al (2018) Polyimide for silicon solar cells with double-sided textured pyramids. Sol Energy Mater Sol Cells 183(October 2017):200–204. https://doi.org/10.1016/j.solmat.2018.03.015
28. Hsu WC et al (2016) Mismatched front and back gratings for optimum light trapping in ultra-thin crystalline silicon solar cells. Opt Commun 377:52–58. https://doi.org/10.1016/j.optcom.2016.04.055
29. Werner J et al (2016) Efficient near-infrared-transparent perovskite Solar cells enabling direct comparison of 4-terminal and monolithic perovskite/silicon tandem cells. ACS Energy Lett 1(2):474–480. https://doi.org/10.1021/acsenergylett.6b00254
30. Werner J et al (2016) Parasitic absorption reduction in metal oxide-based transparent electrodes: Application in perovskite solar cells. ACS Appl Mater Interfaces 8(27):17260–17267. https://doi.org/10.1021/acsami.6b04425
31. Löper P et al (2015) Organic-inorganic halide perovskite/crystalline silicon four-terminal tandem solar cells. Phys Chem Chem Phys 17(3):1619–1629. https://doi.org/10.1039/c4cp03788j
32. Bailie CD et al (2015) Semi-transparent perovskite solar cells for tandems with silicon and CIGS. Energy Environ Sci 8(3):956–963. https://doi.org/10.1039/c4ee03322a
33. Ramírez Quiroz CO et al (2018) Balancing electrical and optical losses for efficient 4-terminal Si-perovskite solar cells with solution processed percolation electrodes. J Mater Chem A 6(8):3583–3592. https://doi.org/10.1039/c7ta10945h
34. http://www.silvaco.com/
35. Hazeghi F et al (2019) Simulation of perovskite solar cells by using CuSCN as an inorganic hole-transport material. Mater Res Express. https://doi.org/10.1088/2053-1591/ab2f1b
36. Hao F, Stoumpos CC, Chang RPH, Kanatzidis MG (2014) Anomalous band gap behavior in mixed Sn and Pb perovskites enables broadening of absorption spectrum in solar cells. J Am Chem Soc 136(22):8094–8099. https://doi.org/10.1021/ja5033259
37. Samiee M et al (2014) Defect density and dielectric constant in perovskite solar cells. Appl Phys Lett 105(15). https://doi.org/10.1063/1.4897329
38. Oga H, Saeki A, Ogomi Y, Hayase S, Seki S (2014) Improved understanding of the electronic and energetic landscapes of perovskite solar cells: High local charge carrier mobility, reduced recombination, and extremely shallow traps. J Am Chem Soc 136(39):13818–13825. https://doi.org/10.1021/ja506936f
39. Ramli NF et al (2018) Model development of monolithic tandem silicon-perovskite solar cell by SCAPS simulation. AIP Conf Proc 1838(January):2017. https://doi.org/10.1063/1.4982178

40. Zhang Y, Blom PWM (2011) Electron and hole transport in poly(fluorene-benzothiadiazole). Appl Phys Lett 98(14):2011–2014. https://doi.org/10.1063/1.3574907
41. Mohottige RN (2020) Numerical simulation of a new device architecture for CIGS-based thin-film solar cells using 1D-SCAPS simulator. J Photochem Photobiol A Chem. https://doi.org/10.1016/j.jphotochem.2020.113079
42. Shawky T, Aly MH, Fedawy M (2021) Performance analysis and simulation of c-Si/SiGe based solar cell. IEEE Access 9:75283–75292. https://doi.org/10.1109/ACCESS.2021.3080391
43. Taube WR, Kumar A. Simulation and optimization of n-type PERL silicon solar cell structure. J Nano- Electron Phys 3(1):1127
44. Kumar A, Ranjan P (2021) Computational analysis of chalcogenides as an inorganic hole transport layer in perovskite solar cells. Opt Quantum Electron 53(9). https://doi.org/10.1007/s11082-021-03186-2
45. Saha P, Singh S, Bhattacharya S (2024) FASnI3-based eco-friendly heterojunction perovskite solar cell with high efficiency. Micro Nanostruct 186(August 2023):207739. https://doi.org/10.1016/j.micrna.2023.207739
46. Saha P, Singh S, Bhattacharya S (2023) Efficient and lead-free perovskite solar cells based on defect-ordered methyl ammonium antimony iodide. IEEE Trans Electron Devices 70(3):1095–1101. https://doi.org/10.1109/TED.2023.3235870
47. Rahman SI, Faisal S, Ahmed S, Dhrubo TI (2018) A comparative study on different HTMs in perovskite solar cell with ZnOS electron transport layer, 5th IEEE Reg. 10 Humanit. Technol. Conf. 2017, R10-HTC 2017, vol. 2018-Janua, pp. 546–550. https://doi.org/10.1109/R10-HTC.2017.8289019
48. Hossain MK, Rubel MHK, Toki GFI, Alam I, Rahman MF, Bencherif H (2022) Effect of various electron and hole transport layers on the performance of CsPbI3-based perovskite solar cells: A numerical investigation in DFT, SCAPS-1D, and wxAMPS frameworks. ACS Omega 7(47):43210–43230. https://doi.org/10.1021/acsomega.2c05912
49. Al Taan L, Abdl Ameer MK, Altaan LM (2022) Temperature and illumination intensity effects on the electric parameters of (n-CdSe/p-CdSe) solar cell using SCAPS, no. May [Online]. Available: www.allmultidisciplinaryjournal.com. Accessed 10 Feb 2024
50. BiplavDahal MDR (2023) Exploring the performance of perovskite solar cells with dual hole transport layers via SCAPS-1D simulation. Mater Today Commun 36:106846. https://doi.org/10.1016/j.mtcomm.2023.106846
51. Kim M et al (2016) Band-tail transport of CuSCN: Origin of hole extraction enhancement in organic photovoltaics. J Phys Chem Lett 7(14):2856–2861. https://doi.org/10.1021/acs.jpclett.6b01039
52. Pan L et al (2020) Cu2O photocathodes with band-tail states assisted hole transport for standalone solar water splitting. Nat Commun 11(1):1–10. https://doi.org/10.1038/s41467-019-13987-5
53. Tennakone K et al (1987) Semiconducting and photoelectrochemical properties of n- and p-Type β-CuCNS. Phys Status Solidi 103(2):491–497. https://doi.org/10.1002/pssa.2211030220
54. Hautier G, Miglio A, Ceder G, Rignanese GM, Gonze X (2013) Identification and design principles of low hole effective mass p-type transparent conducting oxides. Nat Commun 4:1–7. https://doi.org/10.1038/ncomms3292
55. Saha P, Singh S, Bhattacharya S (2023) Optimization and formulation of different Hole-Transporting Materials (HTMs) for the performance of eco-friendly Cs_2TiBr_6- based perovskite solar cells. Energy Technol 12. https://doi.org/10.1002/ente.202300991
56. Wu Q et al (2015) Kesterite Cu2ZnSnS4 as a low-cost inorganic hole-transporting material for high-efficiency perovskite solar cells. ACS Appl Mater Interfaces 7(51):28466–28473. https://doi.org/10.1021/acsami.5b09572
57. Yu W et al (2016) Ultrathin Cu2O as an efficient inorganic hole transporting material for perovskite solar cells. Nanoscale 8(11):6173–6179. https://doi.org/10.1039/c5nr07758c
58. Madhavan VE et al (2016) Copper Thiocyanate Inorganic Hole-Transporting Material for High-Efficiency perovskite Solar Cells. ACS Energy Lett 1(6):1112–1117. https://doi.org/10.1021/acsenergylett.6b00501
59. Nazari P, Ansari F, AbdollahiNejand B, Ahmadi V, Payandeh M, Salavati-Niasari M (2017) Physicochemical interface engineering of CuI/Cu as advanced potential hole-transporting materials/Metal contact couples in hysteresis-free ultralow-cost and large-area perovskite solar cells. J Phys Chem C 121(40):21935–21944. https://doi.org/10.1021/acs.jpcc.7b07061
60. Jones MDK, Dawson JA, Campbell S, Barrioz V, Whalley LD, Qu Y (2022) Modelling interfaces in thin-film photovoltaic devices. Front Chem 10(June):1–21. https://doi.org/10.3389/fchem.2022.920676
61. Yagi T, Uraoka Y, Fuyuki T (2006) Ray-trace simulation of light trapping in silicon solar cell with texture structures. Sol Energy Mater Sol Cells 90(16):2647–2656. https://doi.org/10.1016/j.solmat.2006.02.031
62. Wang JZA (1999) A 19.8% efficient honeycomb multicrystalline silicon solar cell with improved light trapping. IEEE Trans. Electron Devices 46(10):1978–1983
63. Wang DL, Cui HJ, Hou GJ, Zhu ZG, Yan QB, Su G (2016) Highly efficient light management for perovskite solar cells. Sci Rep 6(July 2015):1–10. https://doi.org/10.1038/srep18922
64. Alshal MA, Allam NK (2016) Broadband absorption enhancement in thin film solar cells using asymmetric double-sided pyramid gratings. J Electron Mater 45(11):5685–5694. https://doi.org/10.1007/s11664-016-4735-7
65. Zhao J (2011) Passivated emitter rear locally diffused solar cells. Bull Adv Technol Res 41–43
66. Franklin E (2016) Design, fabrication and characterisation of a 24.4% efficient interdigitated back contact solar cell. Prog Photovoltaics Res Appl 24:411–427. https://doi.org/10.1002/pip.2556
67. Dou B et al (2013) Surface passivation of nano-textured silicon solar cells by atomic layer deposited Al2O3 films. J Appl Phys 114(17):10–15. https://doi.org/10.1063/1.4828732
68. Wang KX, Yu Z, Liu V, Cui Y, Fan S (2012) Absorption enhancement in ultrathin solar cells with antireflection and light-trapping nanocone gratings. Opt InfoBase Conf Pap 10–13. https://doi.org/10.1364/pv.2012.pt2c.2
69. Ma H, Wu B, Zhou J, Huang H, Xu X, Wang C (2017) Efficiency enhancement in ultrathin crystalline silicon solar cells with composite surface gratings. Opt. Commun 393(October 2016):207–212. https://doi.org/10.1016/j.optcom.2017.02.057
70. Kerr MJ, Cuevas A, Campbell P (2003) Limiting efficiency of crystalline silicon solar cells due to Coulomb-enhanced Auger recombination. Prog Photovoltaics Res Appl 11(2):97–104. https://doi.org/10.1002/pip.464
71. Richter A, Hermle M, Glunz SW (2013) Reassessment of the limiting efficiency for crystalline silicon solar cells. IEEE J Photovoltaics 3(4):1184–1191. https://doi.org/10.1109/JPHOTOV.2013.2270351
72. Kopecek R et al (2015) Bifaciality: One Small Step for Technology, One Giant Leap for kWh Cost Reduction. Photovoltaics Int, pp. 1–11 [Online]. Available: www.pv-tech.org. Accessed 2 Mar 2024
73. Yalçin L (2013) Performance comparison of c-Si, mc-Si and a-Si thin film PV by PVsyst simulation. J Optoelectron Adv Mater 15:326–334
74. Mori H (1966) Radiation energy transducing device, pp. 2–6 [Online]. Available: https://patentimages.storage.googleapis.com/9a/61/9e/14fb2dc4fdf4c1/US3278811.pdf
75. Liang TS et al (2019) A review of crystalline silicon bifacial photovoltaic performance characterisation and simulation. Energy Environ Sci 12(1):116–148. https://doi.org/10.1039/c8ee02184h

76. Barkhouse DAR, Gunawan O, Gokmen T, Todorov TK, Mitzi DB (2015) Yield predictions for photovoltaic power plants:empirical validation, recent advances and remaining uncertainties. Prog Photovoltaics Res Appl 20(1):6–11. https://doi.org/10.1002/pip
77. SC, Schmela M (2018) Bifacial Solar Technology Report 2018 edition. Tech Rep, TaiYang News
78. (2019) International Technology Roadmap for Photovoltaic (ITRPV), Tenth edition, Tech Rep, VDMA
79. Zhang D et al (2018) High efficiency 4-terminal perovskite/c-Si tandem cells. Sol Energy Mater Sol Cells 188(July):1–5. https://doi.org/10.1016/j.solmat.2018.07.032
80. Jaysankar M et al (2019) Minimizing Voltage Loss in Wide-Bandgap perovskites for Tandem Solar Cells. ACS Energy Lett 4(1):259–264. https://doi.org/10.1021/acsenergylett.8b02179
81. Wang Z et al (2020) 27%-efficiency four-terminal perovskite/silicon tandem solar cells by Sandwiched Gold Nanomesh. Adv Funct Mater 30(4):1–8. https://doi.org/10.1002/adfm.201908298
82. Duong T et al (2020) High efficiency perovskite-silicon tandem solar cells: effect of surface coating versus Bulk Incorporation of 2D perovskite. Adv Energy Mater 10(9):1–15. https://doi.org/10.1002/aenm.201903553
83. Gharibzadeh S et al (2020) 2D/3D heterostructure for semitransparent perovskite solar cells with engineered bandgap enables efficiencies exceeding 25% in four-terminal tandems with silicon and CIGS. Adv Funct Mater 30(19). https://doi.org/10.1002/adfm.201909919
84. Rohatgi A (2020) 26.7% Efficient 4-terminal perovskite-silicon tandem solar cell composed of a high-performance semitransparent perovskite cell and a doped poly-Si/SiOx passivating contact silicon cell. IEEE J Photovoltaics 10(2):417–422. https://doi.org/10.1109/JPHOTOV.2019.2963564
85. Yang D (2021) 28.3%-efficiency perovskite/silicon tandem solar cell by optimal transparent electrode for high efficient semitransparent top cell. Nano Energy 84:105934. https://doi.org/10.1016/j.nanoen.2021.105934
86. Yao Y et al (2022) Phase-stable wide-bandgap perovskites for four-terminal perovskite/silicon tandem solar cells with over 30% efficiency. Small 18(38):1–12. https://doi.org/10.1002/smll.202203319
87. Raza E et al (2023) Heliyon Design and optimization of four-terminal mechanically stacked and optically coupled silicon / perovskite tandem solar cells with over 28 % efficiency. Heliyon 9(2):e13477. https://doi.org/10.1016/j.heliyon.2023.e13477
88. Singh M et al (2023) Crystalline silicon solar cells with thin poly-SiOx carrier-selective passivating contacts for perovskite/c-Si tandem applications. Prog Photovoltaics Res Appl 31(9):877–887. https://doi.org/10.1002/pip.3693
89. Singh M et al (2024) Performance and optimization study of selected 4-terminal tandem solar cells. Sci Rep 14:1–12. https://doi.org/10.1038/s41598-024-62085-0

All artworks created by PowerPoint and the other data drawing created by OriginPro program.